Blöcher, G., Zimmermann, G., Moeck, I., Brandt, W., Hassanzadegan, A., Magri, F. (2010): 3D numerical modeling of hydrothermal processes during the lifetime of a deep geothermal reservoir. - Geofluids, 10, 3, 406-421,

DOI: 10.1111/j.1468-8123.2010.00284.x

# 3D Numerical Modeling of Hydrothermal Processes during the Lifetime of a Deep Geothermal Reservoir

M. G. Blöcher, G. Zimmermann, I. Moeck, W. Brandt, A. Hassanzadegan & F. Magri

GeoForschungsZentrum Potsdam, Telegrafenberg, D-14473 Potsdam, Germany

Potsdam, February 5, 2010

**Abstract**

The f understanding of hydrothermal processes during production in a geothermal system is critical for optimal reservoir management and sustainable utilization. This study addresses the hydrothermal (HT) processes in a geothermal research doublet, consisting of the injection well E GrSk3/90 and production well Gt GrSk4/05 at the deep geothermal reservoir of Gross Schoenebeck (north of Berlin, Germany) during geothermal power production. The reservoir is located between -4050 to -4250 m depth in the Lower Permian of the North East German Basin. Operational activities such as hydraulic stimulation, production (T = 150°C; Q = -75 $m^3$/h; C = 265 g/l) and injection (T = 70°C; Q = 75 $m^3$/h; C = 265 g/l) change the HT conditions of the geothermal reservoir. The most significant changes affect temperature, mass concentration and pore pressure. These changes influence the fluid density, viscosity and rock properties such as porosity, permeability, heat conductivity and heat capacity. In addition, the geometry and hydraulic properties of hydraulically induced fractures vary during the lifetime of the reservoir. A 3D reservoir model was developed based on a structural geological model to simulate and understand the complex interaction of such processes. This model includes a full HT coupling of various petrophysical parameters. Specifically, temperature dependent heat conductivity and heat capacity are considered as well as the pressure, temperature and mass concentration dependent fluid density and viscosity. These parameters were determined by laboratory and field experiments. The results of a 3D thermohaline FE-simulation of the life-cycle performance of this geothermal well doublet indicate the beginning of thermal breakthrough after 3.6 years of utilization. This result is crucial for optimizing reservoir management.

# 1 Introduction

The technical feasibility of geothermal power production from a deep low-enthalpy reservoir will be demonstrated by means of a borehole doublet system consisting of the production well Gt GrSk4/05 and the injection well E GrSk3/90 at the geothermal research site Gross Schoenebeck (40 km north of Berlin, Germany).

The intended injection well was tested to investigate scenarios of enhancing productivity of thermal fluid recovery from roughly -4100 m deep sandstones and volcanics. (Legarth et al. (2005), Reinicke et al. (2005), Zimmermann et al. (2005)). The doublet system was completed with drilling of the production well to a total depth of -4198 m in 2007, which was followed by three stimulation treatments. Hydraulic stimulation is a method of increasing the productivity of a reservoir by inducing artificial fractures through fluid injection. In order to increase the apparent thickness of the reservoir horizon, the production well was inclined in the reservoir section by 48° and was drilled in the direction of the minimum horizontal stress ($S_h = 288°$ azimuth) for optimum hydraulic fracture alignment in relation to the stimulated pre-existing injection well. Hence, the fractures trend 18° NNE along the maximum horizontal stress (Holl et al., 2005).

An appropriate numerical model becomes increasingly important for planning the well path and fracture design, interpreting hydraulic tests and stimulations, and predicting of reservoir behaviour during the time of geothermal power production. This model should include: (i) the reservoir geology and structure, (ii) the geometry of wells and fractures, (iii) the hydraulic, thermal, mechanical and chemical (HTMC) conditions of the reservoir and fractures generated due to changes of the reservoir conditions.

Various simulation software exists that can handle a part of the required parameters, e.g. Eclipse (SCHLUMBERGER, 2008), Geosys (Korsawe et al. (2003), Wang and Kolditz (2005)) and Feflow (Diersch, 2005). For this study, we utilise Feflow, because this software fully supports hydraulic-thermal coupling. However, Feflow cannot be used to simulate mechanical and chemical reservoir behaviour, or to represent dipping structures (e.g., natural fault zones).

In the present study, we describe how to set-up a thermohaline model for enhanced geothermal systems (EGS). We also discuss the following: (i) the use of numerical simulations in interpreting the life-cycle performance of the geothermal research doublet at the drill site Gross Schoenebeck and (ii) the applicability of the Feflow software for geothermal issues, in particular EGS sites. Life-cycle performance is defined here as the reservoir response depending on the scheduled 30 years of production

and injection.

## 2 Reservoir Characterization

### 2.1 Geology

The reservoir is located within the Lower Permian of the North East German Basin (NEGB) between -3815 m and -4247 m below sea level. The reservoir rocks are classified into two rock units from bottom to top: volcanic rocks (Lower Rotliegend of the Lower Permian) and siliciclastics (Upper Rotliegend of the Lower Permian) ranging from conglomerates to fine grained sandstones, siltstones and mudstones. These two main units can be subdivided depending on their lithological properties (Figure 1, Table 1), which is particularly important for the hydraulic-thermal-mechanical (HTM) modelling.

Due to high hydraulic conductivity and porosity, the Elbe base sandstone I and II are the most promising horizons for geothermal power production in the hydrothermal environment like the NEGB. These siliciclastic rocks can generally be characterized as arkosic litharenite and consist mainly of quartz (80 vol%). The quartz grains are often surrounded by iron (III) oxide-rims; calcareous and albitic cements are rarely found. The feldspar content is less than 10 vol%. K-feldspar, sometimes partly albitised, is the dominant feldspar. Rock fragments are less than 10 vol% and are mainly of volcanic origin. Accessory minerals are plagioclase, microcline and mica. Illite and chlorite are the dominant clays (Milsch et al., 2009).

### 2.2 Fault Zones and Natural Fractures

The fault pattern interpreted from 2D seismic data is characterized by major NW-striking faults and NNE-striking minor faults. In the current stress field, the NE-striking faults bear the highest ratio of shear to normal stresses, exhibiting a critically stressed state in the sandstones and a highly stressed state in the volcanic layer. Since critically stressed faults are described as hydraulically transmissive (Barton et al., 1995, 1996), these NNE-striking faults are expected to be the main fluid pathways in the reservoir (Moeck et al., 2008a). The bottom of the production well, drilled in 2006, is in the direct vicinity of a NE-striking, and W-dipping minor fault (Figure 1).

The natural fractures in the reservoir are parallel to NW-striking strike-slip faults and NE- to N-striking normal faults (Moeck et al., 2005). Among these structures, the N- to NE-striking fractures are expected to serve as principal flow paths due to their high slip and high dilational tendency in the current stress field (Moeck et al., 2009).

### 2.3 Hydraulically Induced Fractures

Four induced hydraulic fractures exist in the well doublet (Table 2). At the production well, a waterfrac treatment was applied in the low permeable volcanic rocks with high amounts of water to create long fractures with low aperture. Two gel-proppant treatments were used to stimulate the sandstone sections with cross-linked gels in conjunction with proppants of a certain mesh size. These treatments can be applied in a wide range of formations with varying permeability and a good control of stimulation parameters. At the injection well, two gel-proppant-fracs and two waterfracs were performed and are henceforth referred to as "multifrac" (Zimmermann et al., 2010a).

The dimension (height, half length and aperture (see Table 2)) of all four induced fractures were computed with the 3D fracture simulator FRACPRO (Cleary, 1994) and were verified by field experiments (Zimmermann and Reinicke, 2010; Zimmermann et al., 2010a). FRACPRO software allows the integration of geological background information and takes wellhead pressures, friction and near wellbore tortuosity into account. The multifrac at the injection well ranges vertically from the Elbe base sandstone II to the Havel formation. The 1st gel-proppant frac at the production well ranges from the Elbe base sandstone II to the Elbe base sandstone I. The 2nd gel-proppant frac ranges from the Elbe alternating sequence to the Elbe base sandstone II, and the waterfrac ranges from the Havel formation to the volcanic rocks (Figure 1). The horizontal distances of the 2nd gel-proppant frac, 1st gel-proppant frac and waterfrac at the production well to the multifrac at the injection well are 308 m, 352 m and 448 m, respectively. In addition to the computed dimensions, microseismicity was monitored by a three-axis geophone installed in the injection well at -3735 m during the waterfrac treatment in the production well. The orientation of the seismic events is similar to the maximum horizontal stress direction $S_H = 18.5° \pm 3.7°$ (Kwiatek et al., 2008, 2009). This implies, that induced waterfrac is mainly tensile with the aperture direction along the minimum principal stress and strike direction along the maximum principal stress.

The hydraulic properties of the fractures were computed with FRACPRO, and the transmissibility $TR_{fr}$ of the multifrac at the injection well was verified by a long term injection experiment in 2004 (Zimmermann et al., 2009). By means of this experiment a fracture transmissibility of approximately 1 Dm $\approx$ 9.87E-13 $m^3$ was determined. This transmissibility value was applied to the other fractures based on the FRACPRO simulations. The fracture transmissibility strongly depends on pore pressure (see Section 4.2) and is related to fracture permeability $k_{fr}$ and aperture $a$.

$$TR_{fr} = k_{fr} * a \tag{1}$$

Under the assumption of laminar flow between parallel plates, the fracture permeability is related to fracture aperture $k_{fr} = \frac{a^2}{12}$ and a hydraulic aperture of 0.228 mm was determined by:

$$a = \sqrt[3]{12 * TR_{fr}} \tag{2}$$

Based on the hydraulic aperture the corresponding fracture permeability can be calculated. The hydraulic fracture conductivity $K_{fr}$ defined in the simulation (Table 2) was determined by means of the gravitational acceleration $g$ [m/s$^2$], reference density of the fluid $\rho$ [kg/m$^3$] and dynamic viscosity of the fluid $\mu$ [kg/(m*s)]:

$$K_{fr} = \frac{k_{fr} * \rho * g}{\mu}. \tag{3}$$

Due to different temperatures, a dynamic viscosity of 0.3 mPa*s for the production well and 0.72 mPa*s for the injection well were used.

### 2.4 Wells

The arrangement of the two wells fulfills two important conditions. First, the wells are located in such a way that the pressure in the reservoir does not drop significantly below the initial formation pressure during production. Second, a temperature drop in the production well should be avoided. The two wells have a distance of 28 m at the surface. Due to the fact that both wells are starting from the same drill site and the injection well is vertically orientated, the production well had to be deviated to ensure a distance of 500 m between both wells within the reservoir. At the top of the reservoir (-3815 m), the inclination is 18° and increases progressively to 48° at -4236 m. Therefore, the distance between the two wells increases from 241 to 470 m from top to bottom of the reservoir (Figure 1).

### 2.5 Mechanical Properties

Moeck et al. (2008b) and Moeck et al. (2009) have presented a stress state determination for the Lower Permian (Rotliegend) reservoir with an integrated approach of 3D structural modelling, 3D fault mapping, stress ratio definition based on frictional constraints, and slip-tendency analysis. The results indicate stress ratios of the minimum horizontal stress $S_h$ being greater or equal to 0.55 times the vertical stress $S_V$ ($S_h \geq 0.55 S_V$), and $S_H \leq 0.78 - 1.00 S_V$ for the maximum horizontal stress, which collectively indicate stress regimes from normal to strike slip faulting. Thus, acting stresses in the 4035 m deep reservoir are $S_V$ = 100 MPa, $S_h$ = 55 MPa and $S_H$ = 78-100 MPa. These stress

ratios were supported by analysis of borehole breakouts in the injection well (Moeck and Backers, 2006).

Holl et al. (2005) determined a stress direction of $S_H = 18.5° \pm 3.7°$ in the Rotliegend at Gross Schoenebeck. This stress direction correlates to the world stress map (Zoback, 1992) and was supported by further analysis of borehole breakouts in the NEGB (Roth and Fleckenstein, 2001).

The pore pressure of the reservoir is $p_p = 43.8$ MPa, determined by p,T-logs at stationary conditions of the geothermal target horizon (Legarth et al., 2005). According to the stress relation of normal faulting ($S_V = S_1$), the effective vertical stress $S_{Veff} = S_1 - p_p = 56.2$ MPa and the effective mean stress $S_{meff} = (S_1 + S_2 + S_3)/3 - p_p = 41.2$ MPa can be calculated.

Besides the stress condition, the elastic moduli for homogeneous isotropic materials were determined by ultra sonic and density logs. The Youngs Modulus (E) for the sandstone and for the volcanic rocks is 55 GPa, and the Poisson's ratio ($\nu$) is 0.18 and 0.2, respectively (Zimmermann et al., 2010a).

### 2.6 Hydraulic Properties

During geothermal power production using a borehole doublet consisting of a production and injection well, the reservoir conditions will change. Besides a temperature decrease at the injection well resulting in a thermoelastic response, the pore pressure will also vary. The initial pore pressure of the reservoir is $p_p = 43.8$ MPa. Assuming a productivity index PI = 13-15 $m^3$/(h*MPa) determined from well testing (Zimmermann et al. (2010a), Zimmermann et al. (2010b)) and a target injection/production rate of 75 $m^3$/h, a pore pressure change of $p_p = 43.8$ MPa $\pm$ 5 MPa can be calculated. This leads to a poroelastic response of the reservoir rocks depending on effective pressure $p_{eff}$ (the difference between confining pressure $p_c$ and pore pressure $p_p$). Consequently, the poroelastic respones will result in a change in permeability $k$ (Al-Wardy and Zimmerman, 2003) and porosity $\phi$ (Carroll and Katsube, 1983; Zimmerman, 1991). Although the minimum horizontal stress $S_h$ is 55 MPa, the confining pressure $p_c$ was approximated by the mean stress $S_m = 85$ MPa. According to $p_{eff} = p_c - p_p$, an effective pressure change of $p_{eff} = 41.2$ MPa $\pm$ 5 MPa can be assumed.

To show the influence of the poroelastic response of Rotliegend sandstone, we investigated the porosity and permeability dependence on effective pressure by laboratory experiments (Blöcher et al., 2009). During the laboratory experiments, the porosity decreases by 6.2% as $p_{eff}$ increases from 5 to 37 MPa, and the permeability decreases by 21.3% as $p_{eff}$ increases from 3 to 30 MPa. The most significant changes occur at low effective pressures up to 20 MPa (Figure 2). At effective pressures above 20 MPa, the porosity changes by less than 0.8%, and the permeability changes by less than 2.3%

as $p_{eff}$ changes by 5 MPa. Therefore the porosity and permeability dependence on effective pressure can be excluded from the numerical investigation.

The initial hydraulic condition of the injection well was tested with a production test of the entire open hole section between -3815 m and -4236 m in 2001 (Legarth et al., 2005; Zimmermann et al., 2009), and a productivity index of 0.97 $m^3/(h\ MPa)$ at maximum pressure drawdown was determined. From the shut-in period transmissibility $TR$ between 4E-14 $m^3$ and 6E-14 $m^3$ was derived. The coefficient of transmissibility is equivalent to the coefficient of permeability $k$ multiplied by the thickness of the aquifer. A performed flow log only showed outflow of the conglomerates and the volcanic sections; the sandstone section was not permeable, potentially due to mud infiltration during the long standstill period of the well. Therefore, the value reflects the transmissibility of the conglomerates and volcanic rocks only. Since the rock matrix of the conglomerates and the volcanic rocks is nearly non-conductive, fluid flow occurs in the natural fracture system solely. For the sandstone layer, the influence of the natural fracture system on the rock conductivity is less pronounced, and matrix flow is the dominant process. The total thickness of conglomerates and volcanic rocks is 136 m. From that a permeability $k$ of 2.9E-16 $m^2$ to 4.4E-16 $m^2$ is obtained (compare Table 3).

In addition, neutron porosity measurements from Reservoir Saturation Tool logs (RST) were used to estimate permeability by applying the empirical formula by Pape et al. (2000) based on a fractal approach. This results in minimum permeability of 3.9E-17 $m^2$ for volcanic rocks and maximum permeability of 1.1E-13 $m^2$ for Elbe base sandstone. This calculation was repeated with porosity data from density and sonic measurements and led to transmissibilities in the range from 2.5E-13 to 6.9E-13 $m^3$ for the 107 m thick sandstone layer (-4004 to -4111 m). By means of the determined transmissibility and thickness of the sandstone layers, permeability ranging from 2.3E-15 $m^2$ to 6.5E-15 $m^2$ was calculated (Table 3). These porosity $\phi$ and permeability $k$ data were verified by abundant porosity (290 samples) and permeability measurements (109) on cores (Trautwein and Huenges, 2005), and the derived physical parameters which were assigned to the stratigraphic layers are listed in Table 3. Further, a ratio between vertical and horizontal permeability of $\frac{k_z}{k_{xy}} = 0.25$ was determined by the core measurements and was assigned to the reservoir model.

FeFlow software requires hydraulic conductivity $K$ [m/s] values of the solid rock (Table 3). Hydraulic conductivity is related to permeability tensor $k$ [$m^2$], gravitational acceleration $g$ [$m/s^2$], reference density of the fluid $\rho$ [$kg/m^3$], and dynamic viscosity of the fluid $\mu$ [kg/(m*s)]:

$$K = \frac{k * \rho * g}{\mu}. \tag{4}$$

The dynamic viscosity of the fluid is commonly regarded as a function of mass concentration $C$ of one or more species (here the value of total dissolved solids (TDS) was used) and temperature $T$ (Diersch, 2002):

$$f_\mu = \frac{\mu_0}{\mu} = \frac{1 + 0.7063\varsigma - 0.04832\varsigma^3}{1 + 1.85\omega - 4.1\omega^2 + 44.5\omega^3}, \tag{5}$$

with mass fraction and relative temperature coefficient

$$\omega = \frac{C}{\rho}, \varsigma = \frac{T - 150}{100}. \tag{6}$$

The following equation of state (EOS) shows that the fluid density is also related to temperature $T$, pressure $p$ and concentration $C$.

$$\rho_f = \rho_{f_0}\left(1 - \beta(T - T_0) + \gamma(p - p_0) + \frac{\alpha}{C_S - C_0}(C - C_0)\right) \tag{7}$$

with thermal expansion coefficient $\beta = \beta(T, p)$, compressibility $\gamma = \gamma(T, p)$ and density ratio $\alpha = \alpha(T, p, C)$, all related to temperature, pressure and concentration (Magri et al., 2005). Therefore, the flow and transport equations for thermohaline convection are non-linear and strongly coupled since temperature, pressure and salinity control the fluid density.

During geothermal power generation, a production temperature of 150°C and an injection temperature of 70°C are scheduled. To include the viscosity dependence on temperature and concentration, we adjusted the hydraulic conductivity $K$ as follows: For the matrix, the hydraulic fractures at the production well and the production well itself, a dynamic viscosity of 0.3 mPa*s (at $T = 150$°C and $C = 265$g/l), and for the cooler injection well and the hydraulic fracture a dynamic viscosity of 0.72 mPa*s was determined (at $T = 70$°C and $C = 265$g/l).

To calculate the dynamic change of fluid density during reservoir utilization for geothermal power generation, we implemented equation 7 into the Feflow environment. The following reference values for concentration $C_0 = 0$ g/l, $C_S = 350000$ mg/l, pressure $p_0 = 100$ kPa and temperature $T_0 = 0°C$ were set. The density equation of state was adjusted by means of sodium chloride concentration, but as shown in Section 2.8, the reservoir fluid is composed by a mixture of calcium and sodium chloride. Therefore, we performed density and viscosity measurements of calcium- and sodium chloride brine at various state points ($C = 0$ to 292 g/l; $T = 20$ to 80°C) and compared the results to the calculations. Due to the fact that the density relation takes only the TDS (Total Dissolved Solids) into account, the calculated data match the measurements very well. Therefore, we calculated the viscosity and density

dependence on pressure, temperature and concentration as shown in Figure 3.

### 2.7 Thermal Properties

According to the continental geothermal gradient at this site, the lowest temperature of the reservoir can be found in the Hannover formation at 137.5°C and increases continuously to 150°C into the volcanic rocks (Henninges et al., 2005). Further parameters are the heat conductivity $\lambda$ and the volumetric heat capacity ($VHC$). For both parameters separate values for fluid (f) and solid (s) phases are required and the bulk (b) property can be calculated by volume fraction-weighted sum as follows:

$$\lambda_b = \phi * \lambda_f + (1 - \phi) * \lambda_s, VHC_b = \phi * VHC_f + (1 - \phi) * VHS_s \tag{8}$$

Due to the low porosity of the reservoir rocks, the properties of the solid fraction are similar to the bulk properties.

The thermal properties of the North East German Basin (NEGB) are well investigated: Lotz (2004) and Scheck (1997) give values for the heat conductivity, Magri (2005) for the heat capacity and Norden et al. (2008) for the surface heat flow. The results of the latter investigations are summarized in Table 3.

Values of the heat conductivity were determined by laboratory experiments at 20°C and were corrected by its temperature dependence. Somerton (1992) has developed the following correlation equation based on experimental data for the prediction of the effects of temperature on heat conductivity on fully saturated sandstones:

$$\lambda(T) = \lambda_{20} - 10^{-3}(T - 293)(\lambda_{20} - 1.38)(\lambda_{20}(1.8 * 10^{-3} * T)^{-0.25\lambda_{20}} + 1.28)\lambda_{20}^{-0.64}, \tag{9}$$

where $\lambda_{20}$ denotes the heat conductivity measured at 20°C by laboratory experiments. Using equation 9, we calculated the heat conductivity of the solid at any point of the reservoir with a defined temperature.

McDermott et al. (2006) have shown that the changes of the fluid's heat capacity at dynamic in situ conditions similar to those of the Gross Schoenebeck reservoir are marginal. Therefore, a constant value during the total time of simulation for the fluid was chosen. The heat capacity of the solid was kept constant as well.

Norden et al. (2008) determined a surface heat flow of $q = 75 \pm 3$ mW/m$^2$ for the Permo-Carboniferous formation at the bottom of the reservoir. By means of a stationary simulation (see

Section 4.1), we compared measured and calculated in situ temperature fields. Best results were generated with a constant heat flow value of $q = 72$ mW/m$^2$.

### 2.8 Chemical Properties of the Formation Fluid

The composition of the formation fluid at the injection well was initially measured before the first stimulation treatment by downhole sampling in January 2001. The samples were taken from the zone of main influx located at the transition of the volcanics to conglomerates and exhibit a TDS (Total Dissolved Solids) of approximately 265 g/l. A pH-value of 5.7 was determined. As shown in Table 4, calcium and sodium are the main cations (with a dominant share of calcium), and chloride is the main anion. Therefore, the formation fluid is classified as Ca-Na-Cl type, which is a typical Rotliegend fluid (Wolfgramm et al., 2003). The analyzed mass fraction (wt%) of calcium, sodium and chloride corresponds to approximately 150 g/l calcium chloride and 100 g/l sodium chloride. The influence of the TDS on density and viscosity was taken into account for the present study.

## 3 Numerical Approach

### 3.1 Governing Equations

Feflow fully implements the governing equation of thermohaline convection in a saturated porous media (Diersch, 2002). These equations are derived from the conservation principles for linear momentum, mass and energy (e.g. Bear and Bachmat (1990), Kolditz et al. (1998)), and the resulting system is given by the following set of differential equations:

$$S_s \frac{\partial h}{\partial t} + \frac{\partial q_{f_i}}{\partial x_i} = Q_\rho, \tag{10}$$

where $S_s$, $q_{f_i}$ and $Q_\rho$ denote specific storage coefficient, Darcy velocity vector and source/sink function of the fluid, respectively.

The Darcy velocity vector can be expressed in terms of hydraulic conductivity tensor $K_{ij}$, fluid viscosity relation function $f_\mu$ and fluid density $\rho_f$:

$$q_{f_i} = -K_{ij} f_\mu \left( \frac{\partial h}{\partial x_j} + \frac{\rho_f - \rho_{f_0}}{\rho_{f_0}} e_j \right). \tag{11}$$

Without adsorption of the solute at the solid surface, the source/sink of the contaminant mass $Q_C$

can be calculated as sum of mass storage, convection, and diffusion (Fickian law):

$$\frac{\partial}{\partial t}(\phi C) + \frac{\partial}{\partial x_i}(q_{f_i} C) - \frac{\partial}{\partial x_i}\left(D_{ij}\frac{\partial C}{\partial x_j}\right) = Q_C, \tag{12}$$

where C is the mass concentration, D the hydrodynamic dispersion and $\phi$ the porosity.

The heat supply $Q_T$ is the sum of heat storage, convection and conduction (Fourier's law) and is determined by means of heat capacity $c$ of the fluid and solid and the thermodispersion tensor $\lambda_{ij}$ (conductive and dispersive part) at certain temperature $T$:

$$\frac{\partial}{\partial t}[(\phi\rho_f c_f + (1-\phi)\rho_s c_s)T] + \frac{\partial}{\partial x_i}(\rho_f q_{f_i} c_f T) - \frac{\partial}{\partial x_i}\left(\lambda_{ij}\frac{\partial T}{\partial x_j}\right) = Q_T, with \tag{13}$$

$$\lambda_{ij} = \lambda_{ij}^{cond} + \lambda_{ij}^{disp} = (\phi\lambda_f + (1-\phi)\lambda_s)\delta_{ij} + \rho_f c_f\left(\alpha_T V_{f_q}\delta_{ij} + (\alpha_L - \alpha_T)\frac{q_{f_i} q_{f_j}}{V_{f_q}}\right) \tag{14}$$

### 3.2 Spatial Discretisation

The horizontal extension of the model is defined by the dimension of the maximum hydrothermal-mechanical influence of stimulation treatments, reservoir utilization by production/injection during power production and geological boundary conditions. Structural geological data are integrated into the model through two northwest-striking faults along the northeast and southwest borders of the reservoir. These faults are no-flow boundaries $q_{n_h}(x_i, t) = 0$ m/s due to a frictional blockade in the current stress field (Moeck et al., 2008b). We defined a model area of 5448 m in an east-west direction and of 4809 m in a north-south direction around the research wells. The vertical extension of a maximum of 594 m is given by geological boundaries, i.e. the Zechstein salt at the top and underlying carboniferous at the bottom. Both rock units are hydraulically non conductive and do not belong to the reservoir rocks.

In order to avoid the accumulation of excessive numbers of elements for such an area, we refined the model in the areas of hydraulically induced fractures and the near well bore region. Consequently, each layer was filled with 18133 6-nodal triangular prisms. Due to the refinement, the edge length of the prism front surface varies between 2.5 m and 400 m in the xy-direction. To keep the ratio between xy and z length close to 1, we performed vertical refinement by subdividing each geological layer into 2 to 10 sub-layers (Table 1), resulting in an average thickness of 16 m. All together, 27 spatial layers consisting of 489591 prism elements and 254744 nodes define the model area (Figure 4).

The induced fractures are represented by 2D quadrilateral vertical elements. These quadrilateral

vertical elements are consistent with the side surfaces of the 6 nodal triangular prisms. Therefore, the vertical extension is 16 m, and the horizontal extension is between 2 m and 3 m.

To represent the vertical injection well, 1D linear vertical elements with a cross sectional area of 126.7 $cm^2$ (diameter $d$=5") were chosen. Due to the fact that the production well is deviated, and that Feflow only supports 1D linear vertical elements, we achieved a short circuit of the three production fractures by arbitrary 1D linear elements. By means of these special 1D elements, nodes of different layers and horizontal positions can be connected without any interaction with the surrounding matrix elements. For the production well, a cross sectional area of 126.7 $cm^2$, corresponding to a diameter of d = 5", was implemented. With Hagen-Poiseuille's law we estimated the hydraulic conductivity of both wells, which are 6867 m/s for injection and 16480 m/s for production well. The discrepancy in hydraulic conductivity in both wells results from a contrast in dynamic viscosity, which are 0.72 mPa*s at 70 °C for the injection well and 0.3 mPa*s at 150°C for the production well.

### 3.3 Time Discretisation

Feflow provides two automatic temporal discretisation techniques: An automatic time step control based on a predictor-corrector scheme of first order accuracy (forward Euler / backward Euler) and a scheme of second order accuracy (forward Adams-Bashforth/ backward trapezoid). The forward Euler / backward Euler time-integration scheme was applied in the following study. For mass transport, we chose Feflow's full upwinding option.

For both the stationary and the transient model, we started with an initial time step length of 1e-08 days. In contrast, the final time of the stationary and transient model varies and was set to 100000 years and 30 years, respectively. The reasons for this decision are described in detail in Section 4.1 and 4.2.

## 4 Application - Simulation of Gross Schoenebeck Site

### 4.1 Stationary State

In preparation of the dynamic reservoir simulation, the initial reservoir conditions have to be determined. These are the initial hydraulic heads, the initial temperature field and the total dissolved solids. For this purpose, we modeled the steady state condition of the natural reservoir without any injection and production and set the initial hydraulic head to $h(x_i, t_0)$ = -185 m for the total domain. The initial temperature $T(x_i, t_0)$ was set to 137.5°C for the total domain, representing the tempera-

ture at the top of the reservoir. For the top layer we applied a constant state temperature of $T(x_i, t)$ = 137.5°C for the total time of simulation. Furthermore, a terrestrial heat flow of $q_{n_T}(x_i, t)$ = 72 mW/m$^2$ was applied to the bottom surface. For the mass concentration we used 265 g/l as a starting value, and no further boundary conditions were set.

As mentioned above, we change the heat conductivity depending on reservoir temperature and the fluid density depending on temperature, pressure and concentration. Due to the fact that these adjustments are dynamic, we needed to calculate the steady state conditions with a transient model as well. The initial time step length of the transient model is 1e-08 days, and the final time was set to 100000 years. After approximately 40000 years quasi stationary conditions were archived. The resulting temperature profile is shown in Figure 5 and is consistent with measured data. Only for the volcanic rocks is the calculated temperature gradient lower than the measured one, possibly an artifact of using a slightly too high heat conductivity. In contrast, the modeled static water level h = -191 m at the injection well matches the measured one h = -182.8 to -196.3 m very well (Huenges and Hurter, 2002).

### 4.2 Transient State

We adjusted the transient model by applying the calculated values for initial hydraulic head, temperature and concentration from the results of the stationary model. In addition, we removed the Dirichlet boundary condition at the top layer, which was a constant temperature of $T(x_i, t)$ = 137.5°C, and added a constant temperature of $T(x_i, t)$ = 70°C along the injection well. This boundary condition represents the temperature of the injected fluid during the total time of the simulation. The final simulation time was set to 30 years according to the expected life-cycle of geothermal utilization.

Further, we applied a constant injection rate of $Q(x_i, t)$ = 75 m$^3$/h at the top of the Elbe base sandstone II unit, which corresponds with the top of the multifrac. A constant production rate of $Q(x_i, t)$ = -75 m$^3$/h was set at the intersection between the production well and the 2nd gel-proppant frac, which is at the top of the Elbe base sandstone II. We set the mass concentration to $C(x_i, t)$ = 265 g/l at the injection point, because the extracted fluid is scheduled to be reinjected after passing a heat exchanger.

The simulation results of the total domain show that the temperature perturbation due to injection does not reach the boundaries of the model. In contrast, pressure perturbations at the northeast and southwest borders of the model could be observed. At the northeast border a pressure build up of 28 m due to injection was simulated. At the farther southwest border a draw down of 4 m due to

production was observed. According to the no-flow boundaries at these borders, we can simulate a water table change without flow across the borders. For the two remaining borders in the northwest and southeast no pressure perturbation was determined.

After starting reinjection of the saline water with a temperature of T = 70°C, the cold water front starts propagating around the injection well. Figure 6 shows different propagation states of the 130°C isosurface during the 30 years (10950 days) of operation time. Figure 8 shows the final state of the hydraulic head, temperature and velocity field after 30 years of production.

Highest fluid velocities can be observed within the induced fractures (Figure 8c) and can result in a pressure equalization. Due to the finite fracture conductivity, significant pressure gradients develop along the fractures (Figure 8a), and their effective length is reduced. The fact that the flow-lines in Figure 7 intersect the multifrac at low angles away from the injection well indicates a combination of linear and radial flow. This results in a non-radial pressure field around the injection well. In contrast, the presence of the multifrac does not have a strong effect on the temperature field, and the temperature drawdown contours around the injection well have predominantly radial symmetry (Figure 6, 8b).

Due to its high permeability, the Elbe base sandstone is the preferred rock for matrix infiltration. After passing the rock matrix, the injected fluid reaches the 2nd gel-proppant frac (308 m away from the injection well). Due to the high hydraulic conductivity of the induced fracture, the fluid is directly channeled to the production well before the cold water front interferes with the production well. After approximately 3.6 years, the cold water front reaches the 2nd gel-proppant frac, and after roughly 5 years, the 1st gel-proppant frac (352 m away the injection well). At the waterfrac (448 m away the injection well) the cooling starts after approximately 10 years. In contrast, the injected cold water will arrive somewhat earlier having heated up along the journey. Figure 7 shows the flow field and the traveling time of the injected water. After approximately 2.5 years, the first injected water reaches the 2nd gel-proppant frac. At this point no significant change in production temperature was observed.

Besides the simulated results of the total domain, we performed a detailed observation of four single points during the time of simulation. The first observation point (OP1) is located at the top of the multifrac in the injection well, and the other three (OP2-4) are at the intersections of the production well and the related induced fracture (Figure 6 and 7). The three hydraulic fractures in the production well are fully connected by the production well, provoking cumulative values of hydraulic head, temperature and concentration at OP2-4. Observation point 4 represents only the properties of the fluid in the production well at the conglomerates, observation point 3 measures the

additional influx of the two Elbe base sandstone units, and observation point 2 gives values for the cumulative flux from the volcanic rocks up to the Elbe alternating sequence.

The chronological behaviour of the four observation points with respect to hydraulic head and temperature are shown in Figure 9. It shows that the hydraulic head build up at the injection well is equivalent to the draw down at the production well, but the absolute value of draw down (388 m) is lower than the value for build up (448 m). By means of the measured productivity index PI = 15 $m^3$/(h*MPa) and an injection/production rate of 75 $m^3$/h, a head level change of 5 MPa can be calculated. According to the density of the fluid, which is 1100 kg/$m^3$ and 1145 kg/$m^3$ at the production and injection well, respectively, water level changes of -463 m in the production and +445 m in the injection well are calculated. The lower simulated values for draw down results from a full connection between well, fracture and reservoir matrix without any skin effects. Therefore, the productivity index inside the Feflow model represents a potential value and is higher than the initial one. We recalculated the productivity index and determined a PI of 17.9 $m^3$/(h*MPa) for the production and a PI of 14.9 $m^3$/(h*MPa) for the injection well well.

In Figure 9, the time history of temperature at the observation points is shown. We excluded observation point four, because the temperature of the injection well is constant at T = 70°C. At the beginning of the simulation, observation points 2 to 4 show different temperatures according to the geothermal gradient calculated by the stationary model. After starting the production, hotter water from the volcanic rocks (OP4) passes observation points 3 and 2. Therefore, an initial increase of temperature at the two gel-proppant fractures is observed. Consequently, an increase in production temperature (OP2) from 144.7°C to 146.3°C can be achieved during the first 10 days of production. Starting from this point, the production temperature remains nearly constant until the cold water front reaches the 2nd gel-proppant frac after 3.6 years. Then, a significant drop of production temperature to 125.8°C at the final simulation time follows. At this discrete point, the temperatures at the 1st gel-proppant frac and in the volcanic rocks are still 133.8°C and 145.6°C, respectively.

It is a well known fact that the hydraulic conductivity of the induced fractures strongly depends on the pore pressure. Although this relation is not implemented in FeFlow, we at least reduced and increased the dimensionless fracture conductivity FCD (Economides and Nolte, 2000) of the induced fractures by an order of magnitude. This mimics to some degree the effects of fracture closure and opening. The dimensionless fracture conductivity FCD is defined as:

$$FCD = \frac{k_{fr} * a}{l_{fr} * k}, \tag{15}$$

where $k_{fr}$, $a$, $l_{fr}$ and $k$ denote fracture permeability, aperture, half length and matrix permeability, respectively. Fracture half length and matrix permeability were kept constant during these simulations. The results, including the fractional influx of the induced fractures, are summarized in Table 5. The chronological behaviour of the production and injection well with respect to hydraulic head and temperature are shown in Figure 10.

In general, for low fracture conductivity (FCD/FCD0 = 0.1), the pressure response of the reservoir is more pronounced. This results in a decrease of the productivity index from 17.7 $m^3$/(h*MPa) to 5.9 $m^3$/(h*MPa). Thus, the waterfrac becomes ineffective, and its fractional influx decreases from 25.1% to 19.4%. Therefore, an initial temperature increase due to the influx of hot water from the volcanic rocks is less pronounced than in the other scenarios. The reduced influx from the volcanic rocks is compensated by an increased influx from the Elbe base sandstone units (1st gel-proppant frac).

For high fracture conductivity (FCD/FCD0 = 10), the productivity index increases from 17.7 $m^3$/(h*MPa) to 25.6 $m^3$/(h*MPa) at the production well. In comparison with the reference simulation, the fractional influx of the induced fractures stays roughly the same. Therefore, the chronological behaviour of the production temperature is similar to the reference results.

## 5 Discussion

A pressure and temperature anomaly occurs at the bottom of the multifrac (Figure 11) at the injection well after 10 days of simulation time. This anomaly is positioned around the injection well in the direction of the induced fractures and is limited to the volcanic rock layer, which is located two spatial layers below the fracture. After 110 days a temperature increase with a maximum value of T = 166°C and a hydraulic head decrease from -175 m to -230 m was observed at this point. Starting from this point, the anomaly decreases and finally disappears after 3 years of simulation time. The anomaly occurs due to the high thermal and hydraulic gradients in combination with the spatial and time discretisation at this specific location. Therefore, we tested the behaviour of the anomaly by varying spatial and time discretisation. Different discretisation techniques influence the time of appearance of the anomaly, but not its magnitude significantly. As mentioned in the spatial discretisation section, the ratio between the horizontal and vertical dimension should be close to 1. Due to the refinement around the wells, a ratio of 0.16 could be achieved. To increase this ratio, more vertical sub-layers have to be implemented, but this will result in an increase of finite elements (6 times more than the current number). Therefore, we decided to increase the number of elements until the magnitude of

the temporary anomaly was less than 10% of the hydraulic head and the absolute temperature value. The spatial and time discretisation at the production well is similar to that of the injection well. In contrast, no high thermal gradients occur at the production well, and even the hydraulic gradient is lower. Therefore, no anomaly at the production well could be observed.

Compared with measurements from the reservoir, the simulation results revealed some limiting options in the modelling procedure. A major limitation may be the restricted implementation of geological structures that are commonly dipping, and thus are non-vertical and undulating. During the hydraulic fracture treatments at the production well in 2007, a direct pressure response in the injection well was observed. The software Feflow cannot handle dipping single structures like fault zones. These fault zones may explain the direct pressure response from one well to the other for fluid injection during stimulation. A set of north to northeast striking faults, known from the 3D structural model and presumably reactivated or dilated by the fluid pressure increase during stimulation, may have acted as connecting structures between both wells causing the instantaneous pressure response in the neighboring well. These structures act as important hydraulic elements, but are not implemented in the current numerical model.

In the present simulation the permeability, porosity and heat capacity were handled as constant values. In the previous section we showed that these properties vary with pressure, temperature and total dissolved solids. According to laboratory experiments, the changes of these parameters are small and can be neglected for the rock matrix. In contrast, the hydraulic conductivity of the induced fractures strongly depends on the pore pressure. This dependence can be implemented in Feflow by changing the fracture properties according to pore pressure change by using the Feflow InterFace Manager (IFM). Pore pressure changes are related to production and injection rates, but an additional change occurs due to changes in the in situ stress field. This mechanical coupling is not part of Feflow, and its influence has to be examined by other simulation software (like Geosys (Wang et al., 2009) or Eclipse (SCHLUMBERGER, 2008)) and verified by field tests.

Using the current FeFlow model, we determined that the first arrival of the cold water front at the production well occurs after 3.6 years. After 30 years of geothermal power production, the temperature of the production fluid is 125.8°C, which is equivalent to a temperature decrease of approximately 19°C. Franco and Villani (2009) have shown that this temperature decrease results in a reduction of power provision by 20% to 30%.

# 6 Conclusions

The primary objective of this paper is to understand the hydrothermal processes occurring in an enhanced geothermal system (EGS) during geothermal power production. Understanding such a geothermal system is critical for optimal reservoir management and sustainable utilization. Therefore, we simulated the hydrothermal conditions of the geothermal research doublet and the related induced fractures at the deep geothermal reservoir of Gross Schoenebeck.

We have shown that a change of the dimensionless fracture conductivity (FCD) of the induced fractures strongly influences the pressure response of the reservoir. For low FCD, the induced fractures become hydraulically ineffective resulting in a decrease of the productivity index. In contrast, the time and the magnitude of the thermal breakthrough was not as affected by the conductivity of the induced fractures. According to these results, an integration of natural fault zones and their pressure-dependent conductivity is the most important issue for further investigations.

With the present simulation, we captured most of the relevant processes for an EGS by means of a thermohaline simulation and by integration of deviated wells and hydraulically induced fractures. The current numerical model displays the reservoir behavior during 30 years of geothermal power production and might be crucial for further reservoir management.

In particular, the numerical model integrates the known reservoir geometry, structural geology, hydrothermal conditions and the relevant coupled processes. The simulation delivers an improved understanding of reservoir behaviour and leads to an interpretation of the stimulation treatments and to a prediction of the long term reservoir characteristics during geothermal power production. Especially, the well path design and the importance of induced fractures can be evaluated. Planning a borehole doublet system is a double edged problem: on one hand, the distance between the wells should be as far as possible to avoid a thermal breakthrough. On the other hand, the wells should be close enough to reduce pressure drawdown in the production well and hence the auxiliary power demand.

For the research doublet system at Gross Schoenebeck, the simulated thermal breakthrough started after 3.6 years production, but the temperature decreases less than 19°C during the prospective 30 years of geothermal power production. Our results may guide reservoir management in its early stages, and with additional new measurements and parameters from the reservoir, the model can be updated to an improved numerical model of ongoing complex processes at the well doublet. Although the current model has some bottlenecks, it has potentially important implications for utilization of

geothermal systems for power production. Exploitation strategies may benefit from focusing on processes indicative of changing reservoir behavior.

## Nomenclature

### Greek symbols

$\alpha$ ..... density ratio [-]

$\alpha_L, \alpha_T$ ..... longitudinal and transversal thermodispersivity [m]

$\beta$ ..... thermal expansion coefficient [1/°C]

$\delta$ ..... Kronecker delta [-]

$\gamma$ ..... compressibility [1/MPa]

$\lambda$ ..... heat conductivity $[W/(m * K)]$

$\mu$ ..... dynamic viscosity [kg/(m*s)]

$\nu$ ..... Poisson's ratio [-]

$\omega$ ..... mass fraction [-]

$\phi$ ..... porosity [-]

$\rho$ ..... density [kg/m$^3$]

$\varsigma$ ..... temperature coefficient [-]

### Roman symbols

$a$ ..... aperture [m]

$C$ ..... mass concentration [mg/l]

$c$ ..... specific heat capacity [J/(kg*K)]

$D$ ..... hydrodynamic dispersion

$d$ ..... well diameter [m]

$e_j$ ..... gravitational unit vector

$FCD$ ..... dimensionless fracture conductivity [-]

$g$ ..... gravitational acceleration [m/s$^2$]

$h$ ..... hydraulic head [m]

$K$ ..... hydraulic conductivity [m/s]

$k$ ..... permeability [m$^2$]

$L$ ..... reference length [m]

$l$ ..... fracture half length [m]

$p$ ..... pressure [MPa]

$Q$ ..... pumping/injection rate of a single well [$m^3/s$]

$q$ ..... surface heat flux [$mW/m^2$]

$Q_\rho, Q_T, Q_C$ .. source/sink function of fluid, heat and contaminant mass [1/s]

$q_{f_i}$ ..... Darcy velocity vector [m/s]

$q_{n_h}$ ..... normal Darcy flux [m/s]

$q_{n_T}$ ..... normal heat flux [$mW/m^2$]

$S_1, S_2, S_3$ ..... maximum, intermediate and minimum principle stress

$S_h, S_H, S_V$ ... minimum and maximum horizontal stress and vertical stress

$S_s$ ..... specific storage coefficient [1/m]

$T$ ..... temperature [°C]

$t$ ..... time [s]

$TR$ ..... transmissibility [$m^3$]

$V_{f_q}$ ..... absolute Darcy flux [m/s]

$VHC$ ..... volumetric heat capacity [$J/(m^3 * K)$]

$x_i, x_j$ ..... position vector

**Subscript** ...

0 ..... value at initial condition ($t = 0$) or reference value

20 ..... value at $T = 20$°C

$b, f, s$ ..... bulk, fluid and solid

$c$ ..... confining

$eff$ ..... effective

$fr$ ..... fracture

$ij$ ..... tensor components

$meff$ ..... effective mean

$p$ ..... pore

$S$ ..... at saturation point

$x, y, z$ ..... coordinates

**Superscripts**

$cond$ ..... conductive part

$disp$ ..... dispersive part

## References


Al-Wardy, W. and Zimmerman, R. W. (2003). Effective stress law for the permeability of clay-rich sandstones. *16th ASCE Engineering Mechanics Conference*, July 16–18, University of Washington, Seattle.

Barton, C., Hickman, S., Morin, R., Zoback, M., Finkbeiner, T., Sass, J., and Benoit, D. (1996). Fracture permeability and its relationship to in situ stress in the dixie valley, nevada, geothermal reservoir. *In: Proceedings of the VIIIth International Symposium on the Observation of the Continental Crust Through Drilling*, February 26- March 2, Tsukuba, Japan, 210-215.

Barton, C., Zoback, M., and Moss, D. (1995). Fluid flow along potentially active faults in crystalline rock. *Geology*, 23:683–686.

Bear, J. and Bachmat, Y. (1990). *Introduction to modeling of transport phenomena in porous media.* Kluwer Academic Publishers.

Blöcher, M. G., Zimmermann, G., and Milsch, H. (2009). Impact of poro-elastic response of sandstones on geothermal power production. *Pure and Applied Geophysics*, special volume:1107–1123.

Carroll, M. and Katsube, N. (1983). The role of terzaghi effective stress in linear elastic deformation. *J. Energy Resour. Tech.*, 105:509–511.

Cleary, M. P. (1994). Critical issues in hydraulic fracturing of high-permeability reservoirs. *SPE paper 27618.*, Proceedings, European production operations conference and exhibition. Aberdeen, Scotland.

Diersch, H. J. G. (2002). Feflow finite element subsurface flow and transport simulation system - user's manual / reference manual / white papaers. *WASY Ltd, Berlin*, Release 5.0.

Diersch, H. J. G. (2005). Wasy software feflow; finite element subsurface flow and transport simulation system. Technical report, Institute for Water Resources Planning and Systems Research, Berlin, Germany.

Economides, M. J. and Nolte, K. G. (2000). *Reservoir stimulation.* Wiley, John & Sons, Incorporated, 3rd edition.

Franco, A. and Villani, M. (2009). Optimal design of binary cycle power plants for water-dominated, medium-temperature geothermal fields. *Geothermics*, In Press, Corrected Proof:–.

Henninges, J., Zimmermann, G., Büttner, G., Schrötter, J., Erbas, K., and Huenges, E. (2005). Wireline distributed temperature measurements and permanent installations behind casing. *Proceedings World Geothermal Congress 2005 Antalya, Turkey, 24-29 April 2005.*

Holl, H. G., Moeck, I., and Schandelmeier, H. (2005). Characterisation of the tectono-sedimentary evolution of a geothermal reservoir implications for exploitation (southern permian basin, ne germany). *Proceedings World Geothermal Congress 2005 Antalya, Turkey, 24-29 April 2005*, pages 1–5.

Huenges, E. and Hurter, S. (2002). In-situ geothermielabor gro schönebeck 2000/2001 : Bohrarbeiten, bohrlochmessungen, hydraulik, formationsfluide, tonminerale. Scientific technical report 02/14, GeoForschungsZentrum Potsdam, Germany.

Kolditz, O., Ratke, R., Diersch, H. J. G., and Zielke, W. (1998). Coupled groundwater flow and transport: 1. verification of variable density flow and transport models. *Adv Water Resources*, 21:27–46.

Korsawe, J., Starke, G., Wang, W., and Kolditz., O. (2003). Finite element analysis of poroelastic consolidation in porous media: mixed and standard approaches. Technical report, University of Hannover, Center for Applied Geosciences, University of Tuebingen.

Kwiatek, G., Bohnhoff, M., Dresen, G., Schulze, A., Schulte, T., Zimmermann, G., and Huenges, E. (2008). Microseismic event analysis in conjunction with stimulation treatments at the geothermal research well gt grsk4/05 in gross schoenebeck/germany. *In: Proceedings of the Thirty-Third Workshop on Geothermal Reservoir Engineering*, Stanford University, Stanford, CA, USA, 7 pp.

Kwiatek, G., Bohnhoff, M., Dresen, G., Schulze, A., Schulte, T., Zimmermann, G., and Huenges, E. (2009). Microseismicity induced during fluid-injection: A case study from the geothermal site at gross schoenebeck, north german basin. *Submitted to J. of Volcanology and Geothermal Research.*

Legarth, B., Huenges, E., and Zimmermann, G. (2005). Hydraulic fracturing in a sedimentary geothermal reservoir: Results and implications. *International Journal of Rock Mechanics and Mining Sciences*, 42:1028–1041.

Lotz, B. (2004). *Neubewertung des rezenten Wärmestroms im Nordostdeutschen Becken.* PhD thesis, FU Berlin.

Magri, F. (2005). *Mechanisms and fluid dynamics driving saline waters within the North East German Basin Results from thermohaline numerical simulations.* PhD thesis, FU Berlin.

Magri, F., Bayer, U., Jahnke, C., Clausnitzer, V., Diersch, H. J., Fuhrman, J. Möller, P., Pekdeger, A., Tesmer, M., and Voigt, H. J. (2005). Fluid-dynamics driving saline water in the north east german basin. *International Journal of Earth Sciences*, 94:1056–1069.

McDermott, C. I., Randriamanjatosoa, A. R., Tenzer, H., and Kolditz, O. (2006). Simulation of heat extraction from crystalline rocks: The influence of coupled processes on differential reservoir cooling. *Geothermics*, 35(3):321–344.

Milsch, H., Seibt, A., and Spangenberg, E. (2009). Long-term petrophysical investigations on geothermal reservoir rocks at simulated in situ conditions. *Transport in Porous Media*, 77, 1, 59–78.

Moeck, I. and Backers, T. (2006). New ways in understanding borehole breakouts and wellbore stability by fracture mechanics based numerical modelling. In *EAGE 68th Conference and Exhibition, 1215 June 2006, extended abstracts volume, CD-ROM, P214*, Vienna, Austria.

Moeck, I., Brandt, W., Blöcher, M. G., Holl, H.-G., Zimmermann, G., Huenges, E., Saadat, A., and Backers, T. (2008a). From gas to geothermal exploration: A case study from the ne-german basin. *In: Extended Abstracts Volume, 70th Conference & Exhibition European Association Geoscientists and Engineers*, 9-12 June, Rome, Italy, abstract D022, CD-ROM.

Moeck, I., Holl, H. G., and Schandelmeier, H. (2005). 3d lithofacies model building of the rotliegend sediments of the ne german basin. *AAPG International Conference & Exhibition*, Paris, France, September 11–14.

Moeck, I., Kwiatek, G., and Zimmermann, G. (2009). Slip tendency analysis, fault reactivation potential and induced seismicity in a deep geothermal reservoir. *Journal of Structural Geology*, In Press, Corrected Proof:–.

Moeck, I., Schandelmeier, H., and Holl, H.-G. (2008b). The stress regime in a rotliegend reservoir of the northeast german basin. *International Journal of Earth Sciences*, ISSN: 1437–3254.

Norden, B., Förster, A., and Balling, N. (2008). Heat flow and lithospheric thermal regime in the northeast german basin. *Tectonophysics*, 460(1-4):215–229.

Pape, H., Clauser, C., and Iffland, J. (2000). Variation of permeability with porosity in sandstone diagenesis interpreted with a fractal pore space model. *Pure appl. geophys*, 157:603–619.

Reinicke, A., Zimmermann, G., Huenges, E., and Burkhardt, H. (2005). Estimation of hydraulic parameters after stimulation experiments in the geothermal reservoir gro schnebeck 3/90 (north-german basin). *International Journal of Rock Mechanics and Mining Sciences*, 42, 7–8:1082–1087.

Roth, F. and Fleckenstein, P. (2001). Stress orientations found in northeast germany differ from the west european trend. *Terra Nova*, 13:290–298.

Scheck, M. (1997). *Dreidimensionale Strukturmodellierung des Nordostdeutschen Beckens unter Einbeziehung von Krustenmodellen.* PhD thesis, FU Berlin; Scientific Technical Report STR97/10, GeoForschungsZentrum Potsdam.

SCHLUMBERGER (2008). Eclipse, reference manual 2008.1. Technical report, Schlumberger Informations Solutions, Business Development Central and Eastern Europe, Hannover, Germany.

Somerton, W. (1992). Thermal properties and temperature-related behavior of rock/fluid systems. *Elsevier*, 257.

Trautwein, U. and Huenges, E. (2005). Poroelastic behaviour of physical properties in rotliegend sandstones under uniaxial strain. *International Journal of Rock Mechanics and Mining Sciences*, 42, 7–8:924–932.

Wang, W. and Kolditz, O. (2005). Object-oriented finite element analysis of thermo-hydromechanical (thm) problems in porous media. Technical report, Center for Applied Geosciences, University of Tuebingen.

Wang, W., Kosakowski, G., and Kolditz, O. (2009). A parallel finite element scheme for thermo-hydro-mechanical (thm) coupled problems in porous media. *Computers & Geosciences*, In Press, Corrected Proof.

Wolfgramm, M., Seibt, A., Hurter, S., and Zimmermann, G. (2003). Origin of geothermal fluids of permo-carboniferous rocks in the ne german basin (ne germany). *Journal of Geochemical Exploration*, 78–79:127–131. Proceedings of Geofluids IV.

Zimmerman, R. W. (1991). *Compressibility of sandstones (developments in petroleum science).*, volume 29, 173 pages. Elsevier Publishing Company.

Zimmermann, G., Moeck, I., and Blöcher, G. (2010a). Cyclic waterfrac stimulation to create an enhanced geothermal system (egs) – conceptual design and experimental results. *Geothermics.*

Zimmermann, G. and Reinicke, A. (2010). Hydraulic fracture stimulation of a deep sandstone reservoir to develop an enhanced geothermal system (egs) - laboratory testing and field experiments. *Geothermics.*

Zimmermann, G., Reinicke, A., Blöcher, G., Moeck, I., Kwiatek, G., Brandt, W., Regenspurg, S., Schulte, T., Saadat, A., and Huenges, E. (2010b). Multiple fracture stimulation treatments to develop an enhanced geothermal system (egs) - conceptual design and experimental results. *Proceedings World Geothermal Congress 2010*, Bali, Indonesia, 25–29 April 2010:5.

Zimmermann, G., Reinicke, A., Holl, H. G., Legarth, B., Saadat, A., and Huenges, E. (2005). Well test analysis after massive waterfrac treatments in a sedimentary geothermal reservoir. In *Proceedings World Geothermal Congress, Antalya, Turkey, 24-29 April 2005, 1-5.*

Zimmermann, G., Tischner, T., Legarth, B., and Huenges, E. (2009). Pressure dependent production efficiency of an enhanced geothermal system (egs) stimulation results and implications for hydraulic fracture treatments. *Pure and Applied Geophysics*, 166, 1089–1106.

Zoback, M. L. (1992). First and second order patterns of stress in the lithosphere: The world stress map project. *Journal of Geophysical Research*, 97:11703–11728.

## List of Tables

## List of Figures

Table 1: Nomenclature for geological formations of Gross Schoenebeck reservoir, including lithology, vertical dimension (below sea level) and numbers of vertical layers used for modeling.

| Unit | Lithology | Top [m] | Bottom [m] | Thickness [m] | spatial Layers |
|---|---|---|---|---|---|
| I Hannover formation | silt- and mudstone | -3815 | -3974 | 159 | 10 |
| IIA Elbe alternating sequence | siltstone to fine grained sandstone | -3974 | -4004 | 30 | 2 |
| IIB Elbe base sandstone II | fine grained sandstone | -4004 | -4059 | 55 | 4 |
| IIC Elbe base sandstone I | fine to medium grained sandstone | -4059 | -4111 | 52 | 3 |
| III Havel formation | Conglomerates from fine sandstone to fine grained gravel | -4111 | -4147 | 36 | 3 |
| IV Volcanic rocks | Andesite | -4147 | -4247 | 100 | 5 |
| **Total** | | **-3815** | **-4247** | **432** | **27** |

Table 2: Dimensions and hydraulic properties of the induced fractures under in situ conditions. The hydraulic conductivity $K_{fr}$ was estimated by means of a reference dynamic viscosity of 0.3 mPa*s for the production well and 0.72 mPa*s for the injection well due to different temperatures.

| well | type | layer | depth [m] | height [m] | half length [m] | $K_{fr}$ [m/s] | a [mm] |
|---|---|---|---|---|---|---|---|
| injection | 2x gel-proppant 2x water | IIB, IIC, III | -4004 to -4147 | 143 | 160 | 0.059 | 0.228 |
| production | water | III, IV | -4098 to -4243 | 145 | 190 | 0.142 | 0.228 |
| production | gel-proppant | IIB, IIC | -3996 to -4099 | 103 | 60 | 0.142 | 0.228 |
| production | gel-proppant | IIA, IIB | -3968 to -4063 | 95 | 60 | 0.142 | 0.228 |

Table 3: Hydraulic and thermal properties of the reservoir rocks under in situ conditions. The hydraulic conductivity was estimated by means of a reference dynamic viscosity of 0.3 mPa*s (at $T = 150°C$ and $C = 265g/l$).

| Unit | $k$ $[m^2]$ | $K$ $[m/s]$ | $\phi$ [%] | $T$ $[°C]$ | $\lambda_s$ $[W/(m*K)]$ | $VHC_s$ $[MJ/(m^3*K)]$ |
|---|---|---|---|---|---|---|
| I | 4.93E-17 | 1.61E-9 | 1 | 138.2 | 1.9 | 2.4 |
| IIA | 1.97E-15 | 6.44E-8 | 3 | 141.7 | 1.9 | 2.4 |
| IIB | 3.95E-15 | 1.29E-7 | 8 | 143.2 | 2.9 | 2.4 |
| IIC | 7.90E-15 | 2.58E-7 | 15 | 145.2 | 2.8 | 2.4 |
| III | 9.87E-17 | 3.22E-9 | 0.1 | 146.5 | 3.0 | 2.6 |
| IV | 9.87E-17 | 3.22E-9 | 0.5 | 147.4 | 2.3 | 3.6 |

Table 4: Composition of Rotliegend fluid at the injection well before first stimulation treatment in 2001.

| cations | [mg/l] | [meq/l] | anions | [mg/l] | [meq/l] |
|---|---|---|---|---|---|
| $Ca^{2+}$ | 54000 | 2694.61 | $Cl^-$ | 167300 | 4718.92 |
| $Na^+$ | 38400 | 1670.29 | $Br^-$ | 300 | 3.75 |
| $K^+$ | 2900 | 74.17 | $SO_4^{2-}$ | 140 | 2.91 |
| $Sr^{2+}$ | 1900 | 43.37 | $HCO_3^-$ | 18.9 | 0.31 |
| $Mg^{2+}$ | 430 | 35.38 | | | |
| $Mn^{2+}$ | 270 | 9.83 | | | |
| $Fe^{2+}$ | 200 | 7.16 | | | |
| $Li^+$ | 204 | 29.39 | | | |
| $Pb^{4+}$ | 180 | 3.48 | | | |
| $NH_4^+$ | 75 | 4.16 | | | |
| $Zn^{2+}$ | 74 | 2.26 | | | |
| $Ba^{2+}$ | 34 | 0.50 | | | |
| $Cu^{2+}$ | 7 | 0.22 | | | |
| $Cd^{2+}$ | 1.8 | 0.03 | | | |
| $As^{3+}$ | 1.4 | 0.06 | | | |
| **Total** | **98677.2** | **4574.91** | | **167758.9** | **4725.90** |
| error of ion balance $= \frac{(\sum cations[meq/l] - \sum anions[meq/l])}{(\sum cations[meq/l] + \sum anions[meq/l])}$ | | | | | **= -0.016** |
| dissolved $SiO_2$ | | | | | **= 80 mg/l** |
| total dissolved solids (TDS) | | | | | **= 266.5 g/l** |
| pH | | | | | **= 5.7** |

Table 5: Simulated fractional influx at the induced fractures for three different FCDs with corresponding pressure response and PI of the production and injection wells.

| | fractional influx | | build up / draw down | PI |
|---|---|---|---|---|
| | $[m^3/h]$ | [%] | $[MPa]$ | $[m^3/(h*MPa)]$ |
| **FCD = 0.1 FCD0** | | | | |
| injection well | 74.4 | 100.0 | 8.6 | 8.7 |
| 2nd gel-proppant frac | 25.9 | 34.7 | | |
| 1st gel-proppant frac | 34.3 | 46.0 | | |
| waterfrac | 14.5 | 19.4 | | |
| production well | 74.6 | 100.0 | -12.6 | 5.9 |
| **FCD = FCD0** | | | | |
| injection well | 73.8 | 100.0 | 5.0 | 14.7 |
| 2nd gel-proppant frac | 26.5 | 35.8 | | |
| 1st gel-proppant frac | 28.9 | 39.1 | | |
| waterfrac | 18.6 | 25.1 | | |
| production well | 74.0 | 100.0 | -4.2 | 17.7 |
| **FCD = 10 FCD0** | | | | |
| injection well | 74.0 | 100.0 | 3.1 | 24.2 |
| 2nd gel-proppant frac | 27.1 | 36.7 | | |
| 1st gel-proppant frac | 28.2 | 38.1 | | |
| waterfrac | 18.6 | 25.1 | | |
| production well | 73.9 | 100.0 | -2.9 | 25.6 |

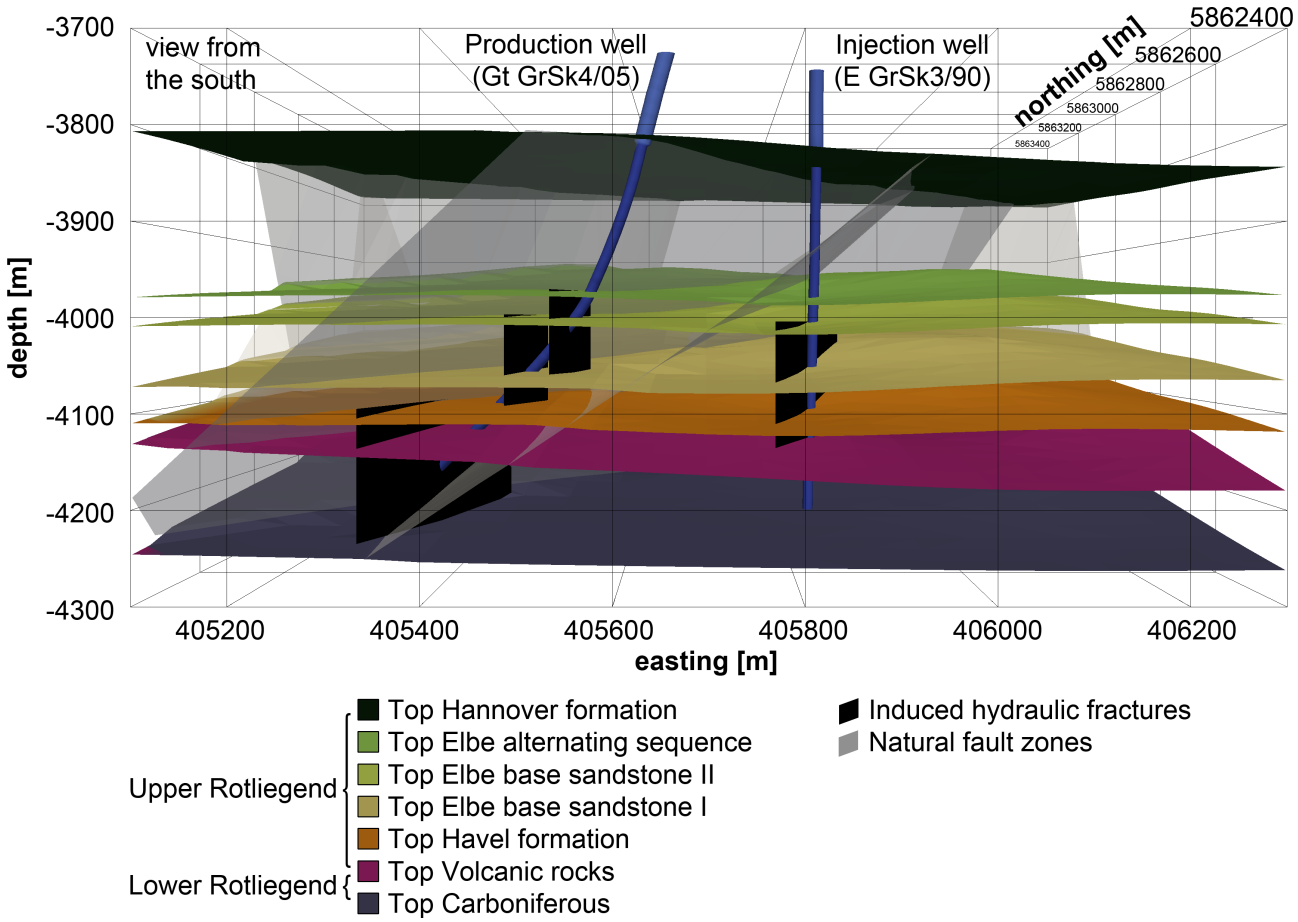


Figure 1: Geological model developed on the basis of 2D seismic and wellbore data. The production well is directed towards a NE-striking/W-dipping fault. The blue tubes indicate the alignment of the well paths, and the black rectangles show the induced fractures of the doublet system at the Gross Schoenebeck site.

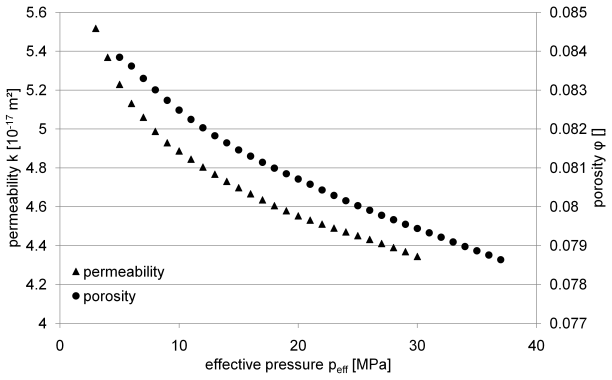


Figure 2: Measured porosity and permeability depending on effective pressure for a Rotliegend sandstone (Flechtinger sandstone, an outcropping equivalent of the reservoir rock).

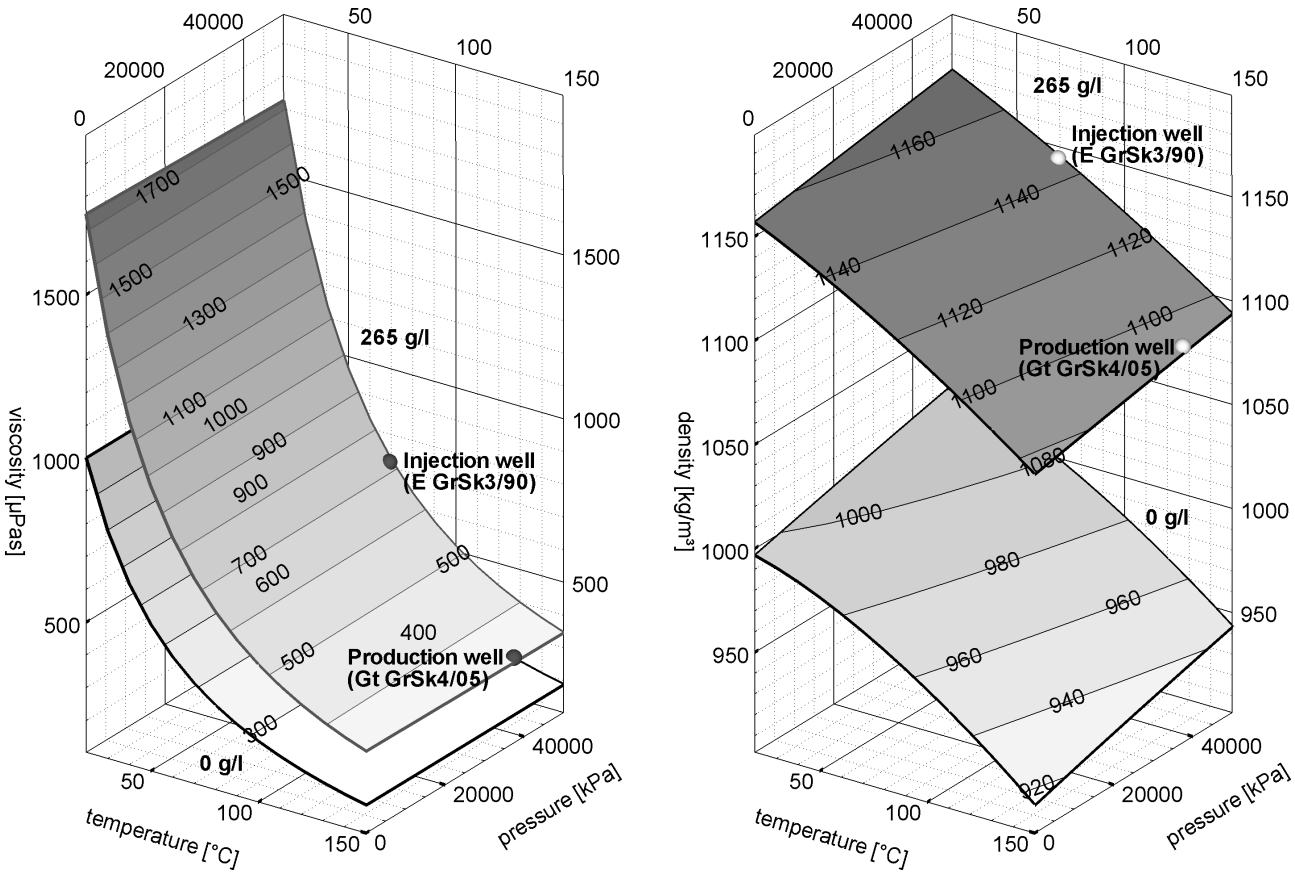


Figure 3: Calculated dynamic viscosity (left) and density (right) of the fluid depending on temperature, pressure and total dissolved solids (TDS). The viscosity and density are significantly different at the specific points of the injection and production well.

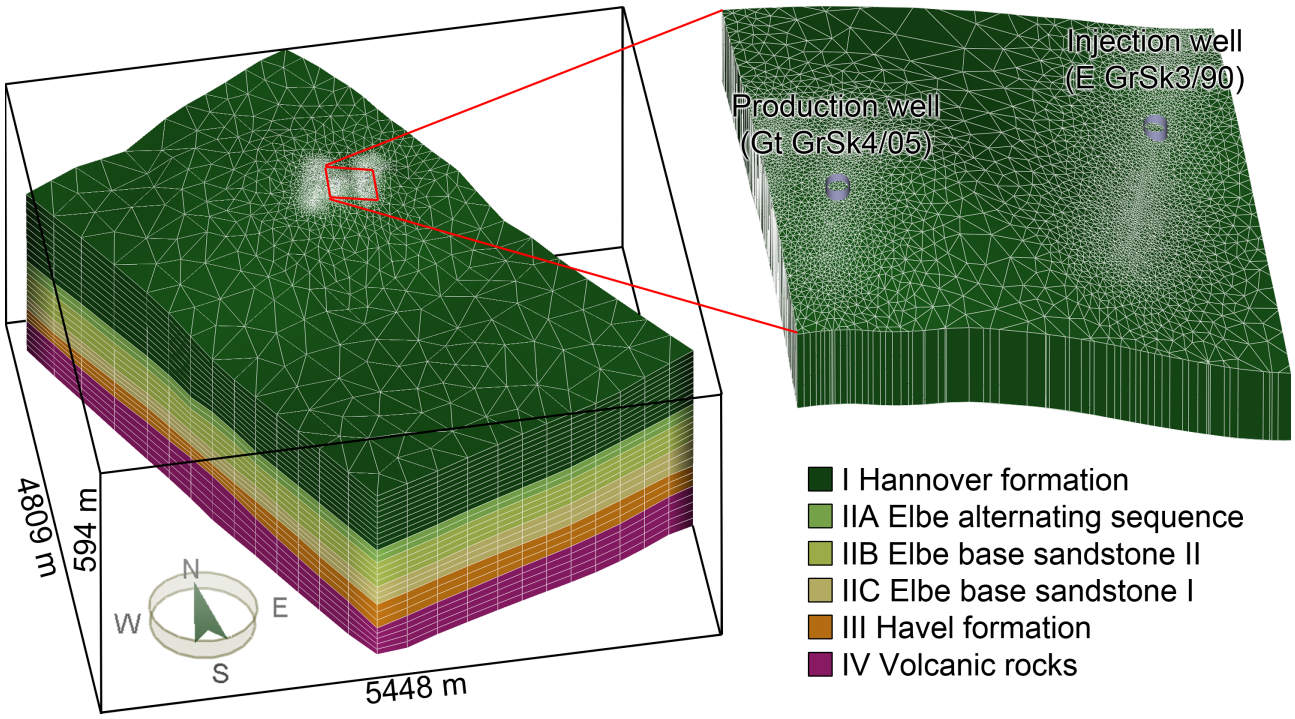


Figure 4: Unstructured reservoir grid consisting of 27 vertical layers, each with 18133 triangular prisms. Together, these 27 vertical layers represent the 6 geological formations.

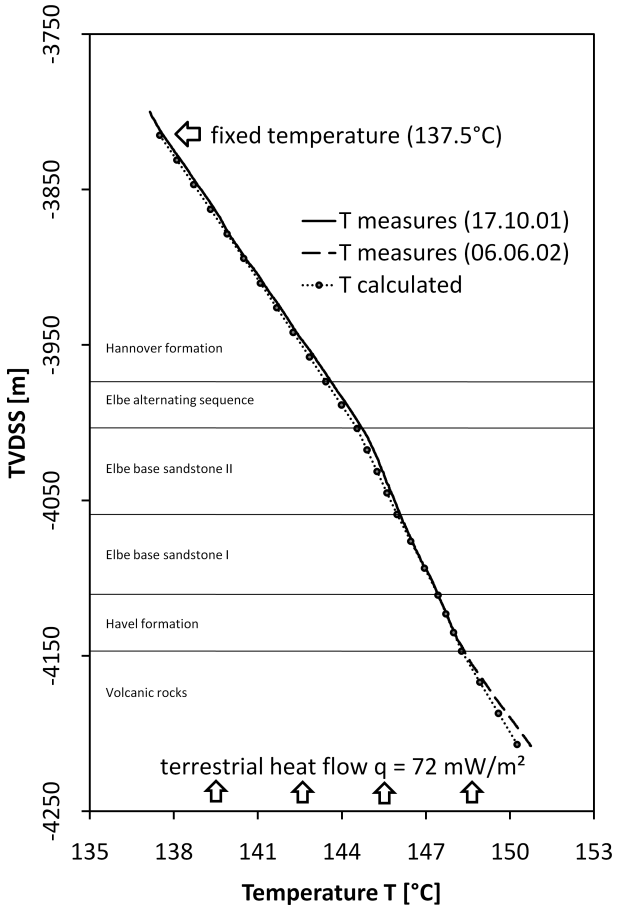


Figure 5: Observed and simulated temperature profile of the reservoir after reopening of the injection well.

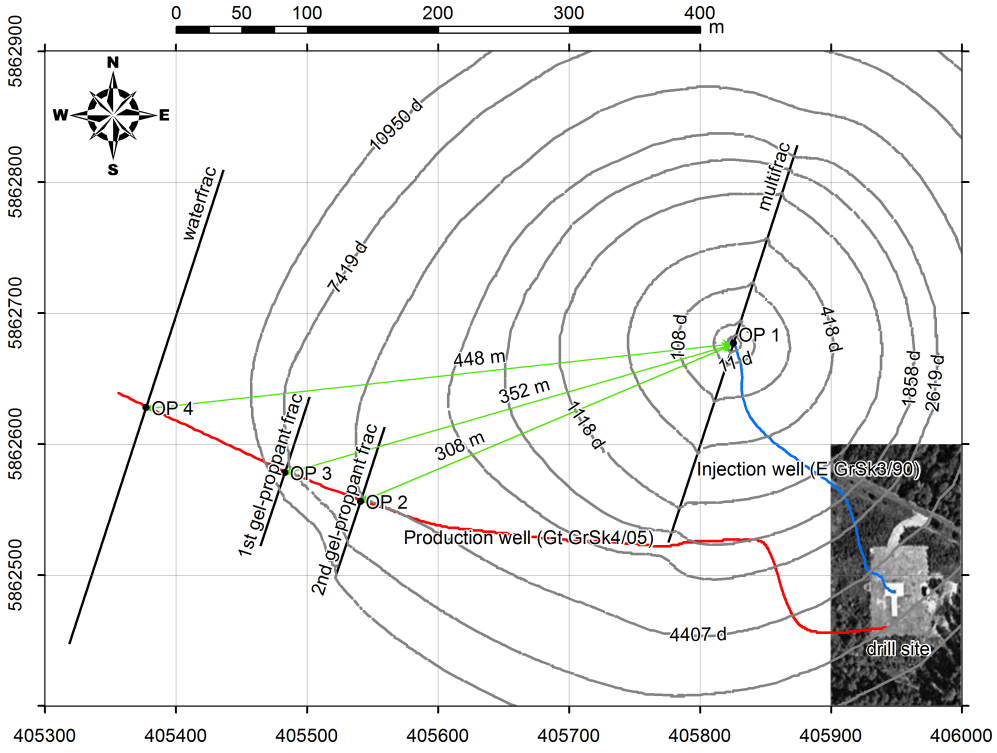


Figure 6: Chronological sequence of the propagation of the 130°C temperature front after start of injection at the Elbe base sandstone I. Also shown is the projection of the drill site Gross Schoenebeck illustrating the well paths of injection well (blue line), production well (red line) and induced fractures.

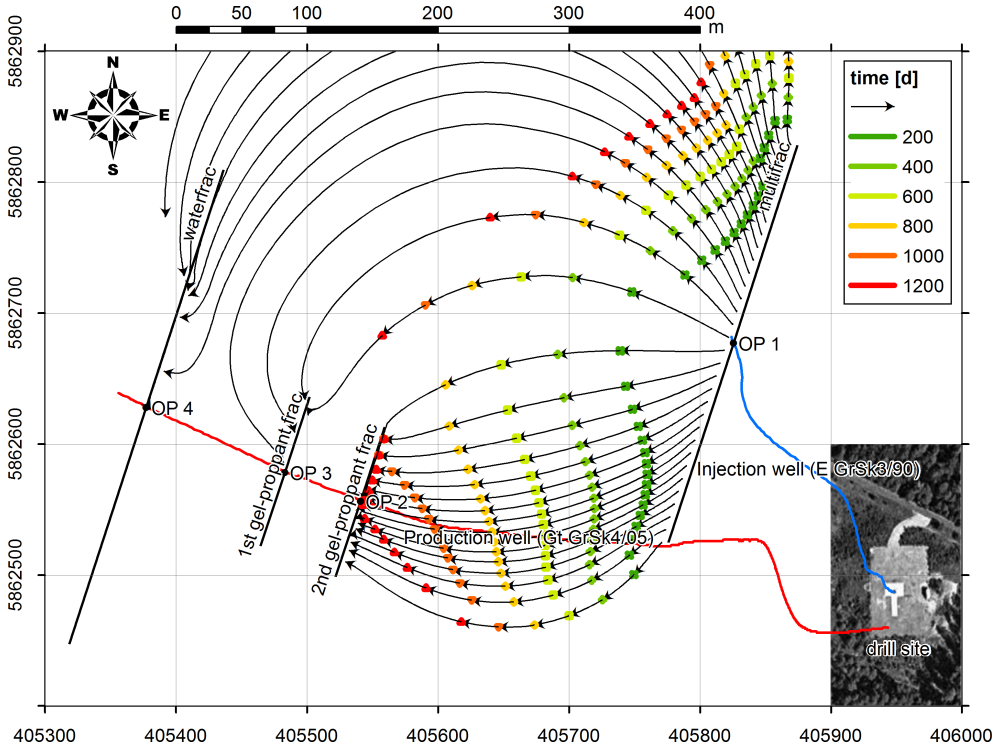


Figure 7: Simulated flow field and traveling time of the injected water after start of injection at the Elbe base sandstone I.

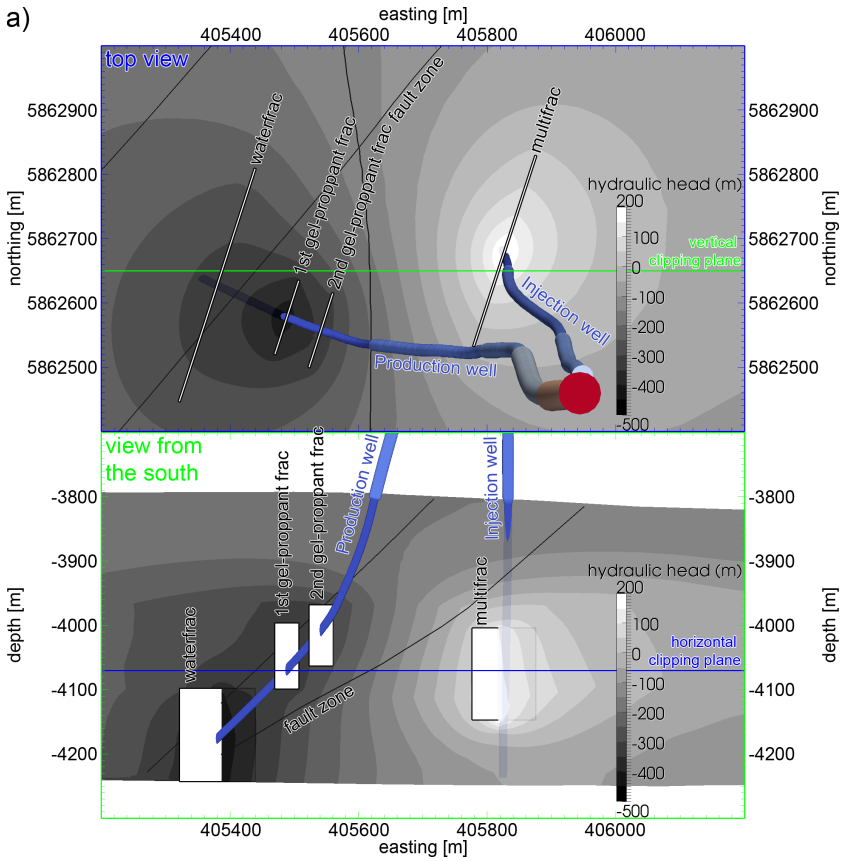
a)
top view
easting [m]
405400
405600
405800
406000
northing [m]
5862900
5862800
5862700
5862600
5862500
waterfrac
1st gel-proppant frac
2nd gel-proppant frac
fault zone
multifrac
hydraulic head (m)
200
100
0
-100
-200
-300
-400
-500
vertical
clipping plane
Injection well
Production well
view from
the south
depth [m]
-3800
-3900
-4000
-4100
-4200
1st gel-proppant frac
2nd gel-proppant frac
Production well
Injection well
multifrac
waterfrac
fault zone
hydraulic head (m)
horizontal
clipping plane

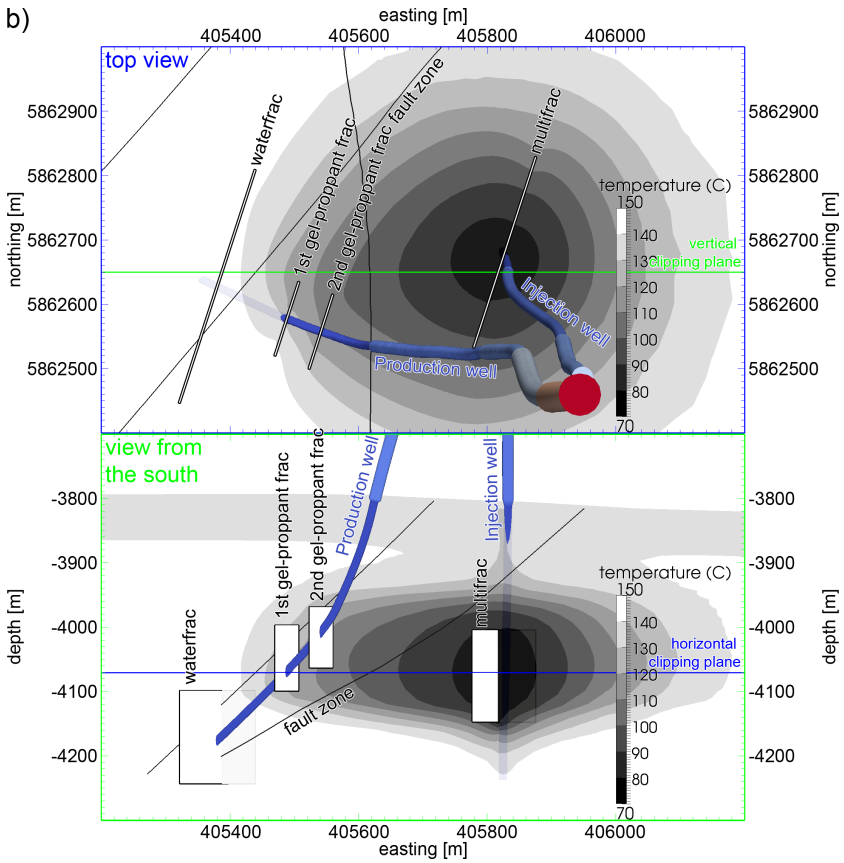
b)
top view
easting [m]
405400
405600
405800
406000
northing [m]
5862900
5862800
5862700
5862600
5862500
waterfrac
1st gel-proppant frac
2nd gel-proppant frac
fault zone
multifrac
temperature (C)
150
140
130
120
110
100
90
80
70
vertical
clipping plane
Injection well
Production well
view from
the south
depth [m]
-3800
-3900
-4000
-4100
-4200
1st gel-proppant frac
2nd gel-proppant frac
Production well
Injection well
multifrac
waterfrac
fault zone
temperature (C)
horizontal
clipping plane

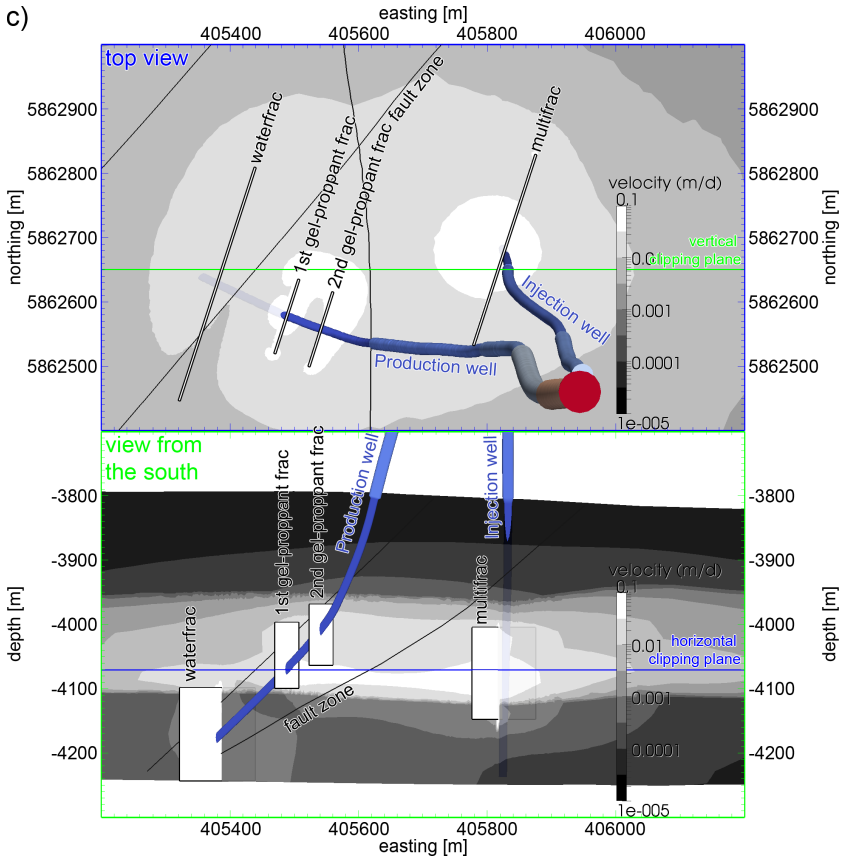


Figure 8: Horizontal cross-section at a depth of -4070 m and vertical cross-section from W to E showing a) hydraulic head distribution, b) temperature distribution and c) velocity field at the final simulation state.

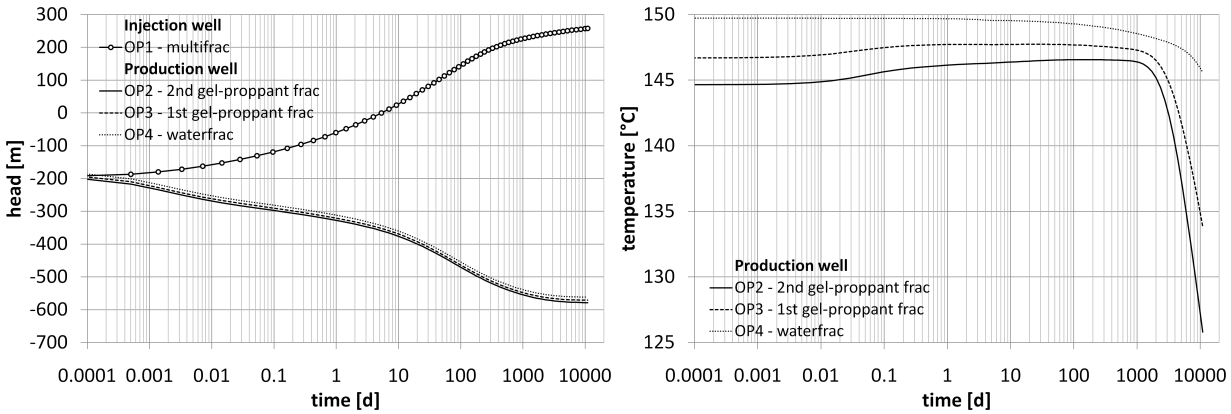


Figure 9: Simulated hydraulic heads (left) at the injection and production well and temperature (right) at the three production fractures during reservoir lifetime.

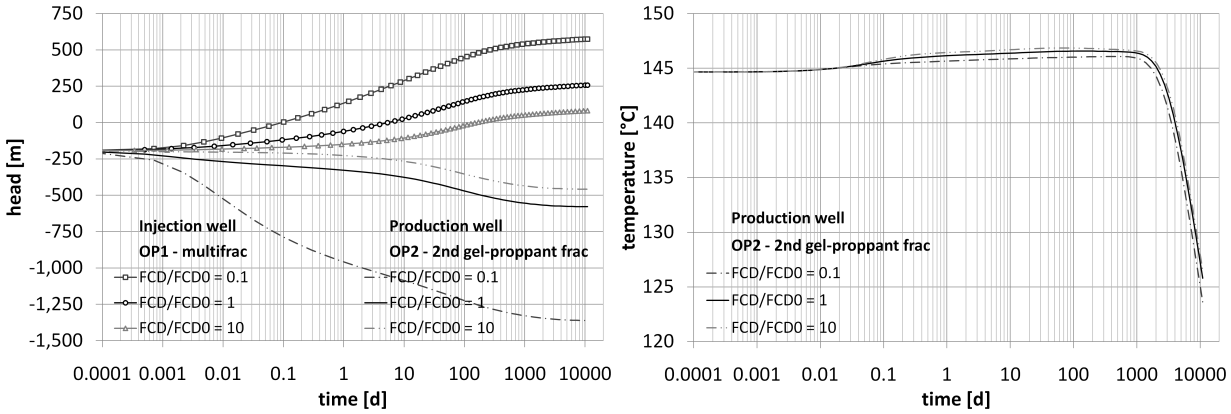


Figure 10: Hydraulic heads (left) at the injection and production wells and production temperature (right) during reservoir lifetime for three different dimensionless fracture conductivities (FCDs).

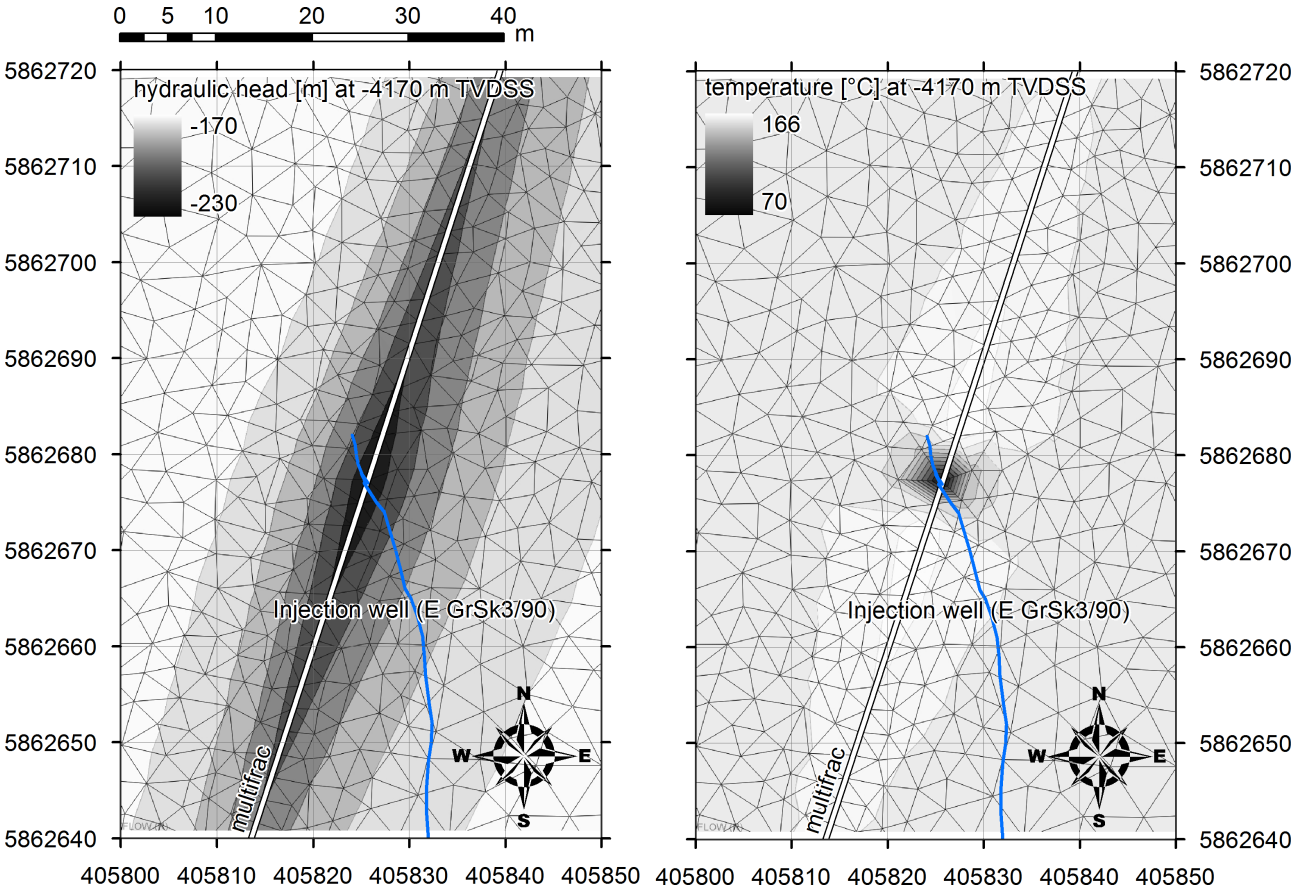


Figure 11: Hydraulic head and temperature anomaly at the bottom of the multifrac at the injection well. Maximum perturbation was observed at -4170 m depth after a simulation period of 110 days.